Available online at www.sciencedirect.com

ScienceDirect

journal homepage: http://www.elsevier.com/locate/acme

Original Research Article

Combining digital image correlation and probabilistic approaches for the reliability analysis of composite pressure vessels

Roberto Garcia-Martin [a], Álvaro Bautista-De Castro [b], Luis Javier Sánchez-Aparicio [b,*], José G. Fueyo [a], Diego Gonzalez-Aguilera [b]

[a] Department of Mechanical Engineering, University of Salamanca, Higher Polytechnic School of Zamora, Campus Viriato, Avenida Requejo, 33, 49022 Zamora, Spain

[b] Department of Cartographic and Land Engineering, University of Salamanca, Higher Polytechnic School of Ávila, Hornos Caleros, 50, 05003 Ávila, Spain

ARTICLE INFO

Article history:
Received 30 July 2018
Accepted 12 October 2018
Available online 14 November 2018

Keywords:
Composite material
Digital image correlation
Full-field strain
Random variable finite element
Stochastic analysis

ABSTRACT

The accuracy of reliability analysis of composite solutions depends on the robust estimation of the uncertainties associated with the mechanical properties of this material. On this basis, we propose a methodology able to exploit the full field strain data provided by the digital image correlation approach in order to extract the probabilistic density functions of the mechanical properties. These probabilistic density functions are complemented by a global sensitivity analysis based on the polynomial chaos expansion and a random variable approach, based on the latin hypercube sampling method, with the aim of obtaining a stochastic evaluation of composite pressure vessels.

1. Introduction

Nowadays, composite materials couple a great part of everyday products such as components for vehicles, aircrafts, marine vessels, lightweight constructions, furniture or food containers among others [1–4]. These type of materials offer better resistance to environmental agents (specially in corrosive atmospheres), a remarkable fatigue endurance and high stiffness-to-weight and strength-to-weight ratios [5,6] and a high energy absorption [7–9]. These properties are specially interesting in those prototypes devoted to the storage of liquefied petroleum or medical gases where the material used to constitute them is steel. Among the limitations of this metallic material are the problems related with corrosion, weight or between the manufacturing process and for which reinforced glass/carbon fibre polymer (GFPR/CFPR) is a potential alternative [10].

Whereas the design of a steel pressure vessel is properly defined and does not entail difficulties due to its homogeneity and isotropic behaviour, the design of composite pressure vessels is not trivial. The heterogeneous nature (e.g. the basic

* Corresponding author.
E-mail address: luisj@usal.es (L.J. Sánchez-Aparicio).
https://doi.org/10.1016/j.acme.2018.10.001

Nomenclature

d	diameter of the circular spot
E	Young's Modulus
υ	Poisson's coefficient
H	height of the ROI
MIG	mean intensity gradient of the speckle pattern
$rand$	random factor to separate the speckle pattern spots
α	indices of the PCE
ψ_α	multivariate polynomial
$\hat{S}_i$ $\hat{S}_i^t$	first-order and total Sobol's indices
$step$	separation between speckle pattern spots
W	width of the ROI

constituents of the composite material, the fibre orientation or the assembly and manufacturing processes) [11], as well as the possibility of being orthotropic or fully anisotropic materials [12], demands the use of numerical simulation, by means of the finite element method (FEM), to study its mechanical behaviour. However, the use of these numerical simulations from a deterministic point of view (numerical simulations on which are adopted a unique variable for the different inputs) cannot provide suitable safety margins for the design of reinforced fibre polymer (FPR) structures [11]. Therefore, it is necessary to incorporate probabilistic approaches able to take into account the uncertainty related with the material, through the use of methods such as random variable models or the so-called random fields method [13]. These approaches take into account these uncertainties at different levels into the numerical model: from constituent levels (micro-scale), ply levels (meso-scale) to component levels (macro-scale) [13]. The use of these stochastic approaches offer advantages in terms of material utilization and would lead to a more accurate reliability estimation [11].

Therefore, the creation of accurate stochastic numerical simulations and the use of this product in an efficient way requires a comprehensive knowledge of the material behaviour. Generally, this evaluation is carried out by means of direct measurements through the use of linear variable differential transformers (LVDTs), laser transducers, extensometers and electrical resistance strain gauges [14–16]. The results of these techniques are highly affected by the presence of cracking, sliding or uneven load distributions without forgetting the local nature of these measurements (especially in the strain gauges) which are not particularly useful in detecting the global response of the material. Apart from these limitations, the use of these direct measurement systems may complicate the preparation of the test, entailing a high cost related to the use of the possible instrumentation (gauges or optical fibres) or to possible damage to sensors [15]. To overcome these drawbacks, several full-field indirect optical techniques have been developed such as Moiré inteferometry [17], particle image velocimetry (PIV) [18] and, digital image correlation (DIC) [19]. This latter methodology has proved to be an efficient technique in composite materials, allowing the characterization of the mechanical properties of the materials, as well as for to studying the displacement and strain distribution during the experimental tests [14,15,20]. However, the full-field capacity of this technique, in displacements and strains, is not exploited in most of the cases, using only part the data provided by two points (similar to an extensometer) to create the stress–strain curves and thus, to extract the mechanical properties of the material [14,15,20–22].

This paper therefore takes into account the influence of the uncertainties in the accurate numerical simulation of composite solutions, as well as the potential offered by the DIC approach: (i) accuracy; (ii) non-contact nature and (iii) full-field of displacements and strains. We propose a method for integrating the uncertainties presented in the mechanical properties of composite materials, extracted by means of the DIC approach, into probabilistic advanced numerical simulations with the aim of evaluating the safety of composite pressure vessels from a probabilistic point of view. To this end, the following structure was used: Section 1 is introduction; Section 2 describes the composite materials used, the digital image correlation method and the experimental methodology carried out in the specimens; Section 3 shows the experimental results obtained by the digital image correlation as well as the characterization of the mechanical properties of the material; Section 4 is dedicated to the integration of the data from the digital image correlation in probabilistic numerical simulations and finally Section 5 discusses the conclusions.

2. Materials and methods

2.1. *Composite solution evaluated*

Specimens used for the study consist of composite manufactured solutions made by an epoxy resin matrix Biresin CR82® with a hardener Biresin CH80-10® (Table 1) and E-Glass fibres composed by a fibre "Taffeta" Woven Roving EWR 300-1250® with a thickness of 0.3 mm (Table 2). The matrix was performed with a proportion of 158 g of resin and 42 g of catalyst for a specific quantity of 200 g.

Prior to performing the matrix, a wooden mould of dimensions 310 × 210 mm was manufactured, placing on it a perimeter tape with a thickness of 2 mm (red tape), in order to set this thickness in the subsequent manufactured specimens. Furthermore, a transparent film was placed on the wooden mould for demoulding (Fig. 1a).

A multilayer taffeta $[0,90]_S$ was performed (Fig. 1c). The first piece of the Woben Roving was placed and properly oriented on the surface of the wooden mould, impregnating it with the matrix (resin and catalyst) through the use of a brush. Subsequently, in the wooden mould we added eight more

Table 1 – Technical specifications of the epoxy resin used.

Mechanical properties	Value
Density (g/cm^3)	1.14
Flexural E-Modulus (MPa)	3600
Tensile E-Modulus (MPa)	3500
Flexural strength (MPa)	130
Elongation at maximum flexural strength (%)	4.6
Tensile strength (MPa)	75
Elongation at maximum tensile strength (%)	3.9
Water absorption (%)	0.23

Table 2 – Technical characteristics of fibres Woben Roving EWR 300-1250.

Glass type	E-Glass
Thickness (mm)	0.3
Density (warp × weft) (end/cm)	4.6 × 4.1 ± 10%
Tex (warp × weft)	300 × 400
Moisture content (%)	0.1% at 20 °C
Loss on ignition (%)	0.4–0.8
Width (cm)	125 ± 1
Weight (g/m^2)	300 ± 15
Weight per roll (kg)	50
Tensile strength (MPa)	3400
Elongation at maximum tensile strength (%)	4.5

layers (Fig. 1a), repeating the impregnation process with the matrix on each one of them. Once the nine fibre layers (the initial fibre layer and the eight fiber layers added) were in place, a paint roller was carefully used on each surface of the wooden mould to remove the surplus matrix in order to avoid displacements of the fibre layers. The time needed for adding the fibre layers on the wooden mould was 50 min.

All fibre layers were progressively pressed in order to achieve the desired thickness established by the red tape (2 mm). Thus, they were dried in a low-temperature furnace about 50 °C for 5 h. As a result, a plate of epoxy resin with a symmetrical fibre reinforced oriented at 90° was obtained. Finally, from this plate a total of five composite specimens were extracted with the measures established by ISO guidelines [23] (Fig. 1b and c). These specimens were cut using a computer numerical control (CNC) machine.

2.2. *Mechanical characterization of the composite solution: the 2D digital image correlation method*

In order to characterize the mechanical properties of the composite solution previously shown, the 2D digital image correlation (2D-DIC) approach was used. This method is an optical non-contact technique for measuring material deformations that uses image registration algorithms to track the relative displacements suffered by material points between a reference state (underformed situation) and the subsequent deformed states during the mechanical tests (Fig. 2a).

For this tracking, it is necessary to acquire several images by means of a digital camera. Then, the reference image, which corresponds with the undeformed state, is split into smaller regions called subsets. These subsets are the features tracked along the different images by means of a cross-correlation coefficient, the Zero mean Normalized Cross-Correlation (ZNCC) being the most used index, since it presents insensitivity to illumination lighting noise [24].

During this tracking, it is assumed that the deformation of the subset can be represented as a linear combination of six degrees of freedom (translation in the *x* and *y*-direction, elongation in the *x* and *y*-direction and shear deformation in the *x* and *y*-direction) with respect to the reference subset (Fig. 2b).

At this point of the methodology, it has been possible to track the deformations suffered by all the subsets with pixel accuracy (cross correlation matching). This accuracy is due to the discrete nature of the digital image (with integer values that range from 0 to 255 in a 8 bits image). With the aim of obtaining a subpixel accuracy, the DIC method uses an iterative non-linear least square optimization scheme. During this optimization, an initial approximation uses the position tracked during the cross correlation stage, and then a b-spline interpolation scheme is used to pass from a discrete space of gray values to a continuous function. Among the types of b-splines methods available nowadays (from bicubic splines to biquintic b-splines), the biquintic b-spline is one of the most accurate [25].

Starting from the continuous space generated by means of the b-spline interpolation, the Inverse Composition Gauss-

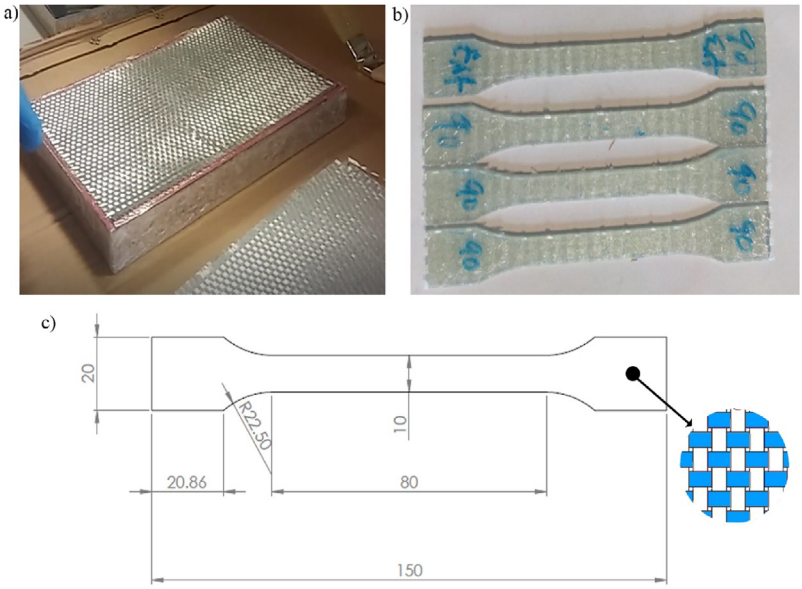

Fig. 1 – Composite solution manufactured: (a) wooden mould with fibre layers symmetrical oriented at 90°; (b) composite specimens prepared for the experimental campaign and; (c) dimensions (in mm) according with the guideline BS EN ISO 527-5:2009 of the composite specimens with a detail of the taffeta configuration.

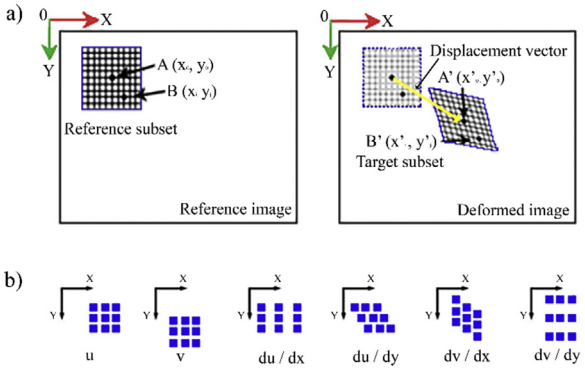

Fig. 2 – Graphical representation of the DIC approach: (a) evaluation of the displacement suffered by a subset and (b) degrees of freedom considered during the displacement analysis. *u* and *v* represents the translation of the subset in the *x* and *y* directions respectively; *du/dx* and *dv/dy* the elongation of the subset in the *x* and *y* axis respectively and; *du/dy* and *dv/dx* the shear deformation of the subset in the *x* and *y* axis respectively.

Newton method (IC-GN) was used to optimize the cost function. On each iteration, the IC-GN algorithm finds a small deformation of the reference subset (underformed image) that best fits the deformed reference subset, then, the shape function, defined by the six degrees of freedom (Fig. 2b), is updated [26]. This process is repeated until a convergence threshold is reached.

The procedure described above is repeated in all the subset that compose the image, allowing a full-field displacement to be obtained. It is worth mentioning that this process is complemented by the reliability guided method proposed by Pan [27]. This approach begins with a selected seed point and proceeds with the neighbour subset with highest ZNCC. Thanks to this, error propagation is avoided [27].

Additionally to the displacement, the DIC method can also determine the strains produced in specimens. In this case the gradients calculated during the previous step, by means of the IC-GN algorithm, are used to compute the Green–Lagrangian strain tensor. This method is applied over the entire region of interest (ROI) in order to obtain the corresponding strain field.

Complementary to the above mentioned and exposed in [24], an accurate extraction of displacements and strains requires the consideration of the following aspects: (i) a proper preparation of the specimen surface and (ii) a geometrical calibration of the camera.

2.2.1. *Specimen preparation*

Under the basis defined previously, the success of the DIC approach depends strongly on the random intensity distribution of the ROI [28,29]. This intensity distribution must present distinct, unique, non-periodic and stable grayscale features, the so-called speckle pattern [28]. This speckle pattern can be natural (texture of the material) or artificial, the last one being the most robust and common [28]. For the present study case, and taking into account the absence of natural texture of the composite specimens, an artificial speckle pattern was applied following the approach proposed by Chen et al. [29].

In a first stage, a regular pattern of circular spots were generated, using as input the diameter of the circular spot (*d*) as well as the separation between circles (*step*). Then, this regular grid was perturbed with a random factor (*rand*). This perturbation avoids the generation of a isotropic pattern with preferential local features (Eqs. (1) and (2)) [29]. Finally, this speckle pattern was printed and applied, through the use of a transfer, on the surface of the specimen. It is worth mentioning that the specimen surface was treated previously with an elastic white primer, allowing us to optimize the contrast and adherence of the speckle pattern (Fig. 3).

$$x = x_i \pm \frac{1}{2} * rand * step \tag{1}$$

$$y = y_i \pm \frac{1}{2} * rand * step \tag{2}$$

where *x*, *y* are the coordinate of the center after the perturbation, x_i, y_i are the coordinates of the center before perturbation, *rand* is a random factor from 0 to 1 and; *step* is the distance between centers.

2.2.2. *Camera calibration*

The images captured by optical sensors suffer from lens distortion that can affect the final accuracy of the results. This error source can be minimized through the use of geometrical calibration algorithms which are able to remove the radial and tangential distortion induced by the lens system in the images acquired. In the present case, the calibration procedure defined by [30] was used. This method follows the next steps [30]: (i) detection of the control points in the raw images through the use of the edge detection and ellipse fitting method; (ii) optimization of the camera parameters and world coordinates of the control points using the Levenberg–

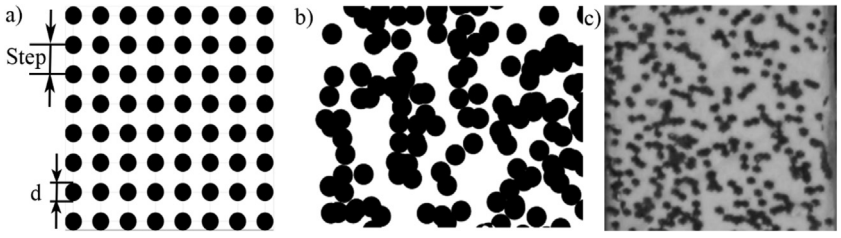

Fig. 3 – Speckle pattern design: (a) regular grid; (b) result of the random perturbation and (c) pattern captured by the camera.

Marquardt algorithm; (iii) extraction of the frontal images and the use of the calculated positions of the control points in the frontal images as an initial approximation in order to refine the positions for the subsequent process in the DIC method (subpixel interpolation and non-linear optimization); (iv) the reverse projection of the detected control points in the frontal images back to the raw images and (v) refinement of the camera parameters together with the world coordinates of the control points.

2.3. *Data acquisition prototype*

In order to carry out the DIC approach, an in-house acquisition prototype was developed. This prototype was built with the following components (Fig. 4): (i) a digital reflex camera Canon EOS 700D with a 60 mm prime macro-lens (Table 3); (ii) a programmable logic controller (PLC) composed by a Raspberry Pi 3® and a Monarco HAT®; (iii) a relay module with eight channels and (iv) a LED lighting unit with 50 W of power.

Regarding the PLC of the prototype, one of its analog inputs was connected with a load cell HBM K-U5-200K-D® of 200 KN from the traction testing machine MTS Alliance RF/200 establishing load set-points (from 0 kN to 10 kN in intervals of 0.5 kN). This test machine has a test speed comprised between 0.01 mm/min and 500 mm/min and an accuracy with an error between 1 N and 2 N, being suitable for the evaluation of the composite solution proposed. Then, these loads were synchronized through the PLC with the camera shots in order to obtain, in the same instant, an image and a load value. Thus, this data is registered through the PLC.

Fig. 4 – Experimental prototype used during the traction tests in the specimens.

Table 3 – Technical specifications of the digital reflex camera Canon EOS 700 D and the macro lens system used.

Canon EOS 700 D	
Sensor type	CMOS APS-C
Sensor size	22.3 × 14.9 mm^2
Crop factor	1.61
Pixel size	4.3 μm
Image size	5184 × 3456 px
Total pixels	18.5 Mpx
Focal length	60 mm
Closer focused distance	254 mm
Lens magnification	1:1 (life size)
Dimensions	133.1 × 99.8 × 78.8 mm

3. Experimental results

3.1. *Tests setup*

The mechanical characterization of the composite specimens developed in Section 2.1 was carried out by means of a 2D-DIC approach. With the aim of obtaining reliable results, a proper test set-up was considered, comprising the following stages: (i) the estimation of the distance and depth of field between the camera and the test specimen; (ii) the application of a speckle pattern on the tests specimens and (iii) the geometrical calibration of the camera.

The resolution of the DIC approach depends strongly on the Ground Sample Distance (GSD) of the images. However, if the camera is close regarding the target (surface with the speckle pattern of the specimen), the depth of field will be lower. On this basis, the acquisition system was placed at 1 m with respect to the traction testing machine (Fig. 5), achieving a GSD of 0.072 mm/px and a depth of field of 0.04 m (the aperture used was 7.1). It is worth mentioning that an ISO-100 and a shutter speed of 1/100 s were used to capture all the images, ensuring the best quality in terms of contrast and sharpness.

Concerning the texture of the specimens, an artificial speckle pattern was generated by means of the methodology proposed in Section 2.2.1. To this end, a regular grid with circular shapes was numerically created with a diameter (*d*) of 0.50 mm and a distance between the centers of the circles (*step*) of 1.22 mm. Then, this regular grid was perturbed adding to the horizontal and vertical coordinates of each blob a random displacement of 0.7 times the GSD (*rand*), resulting in a covering factor of 51% according with the range recommended by Lecompte et al. [31] (40–70%). Finally this speckle pattern was printed and applied on the surfaces of the tests specimens previously treated with an elastic white primer (Fig. 6).

To validate the quality of the speckle pattern applied, the mean intensity gradient (MIG) was calculated as follows [32] (Eq. (3)). Higher MIG values suggest better gray distribution and thus imply lower errors in the final results. As a result an MIG of 46.8 was obtained, assuming it as an acceptable value regarding the quality evaluations of speckle patterns per-

Table 4 – Results obtained from the mechanical characterization of the specimens.

Parameter	Mean	Covariance (%)	Lower bound	Upper bound
Young's Modulus (GPa)	27.00	4.82	23.90	29.80
Poisson's ratio (–)	0.21	33.25	0.18	0.23
Yield strain (mm/mm)	0.021	15.69	0.019	0.023

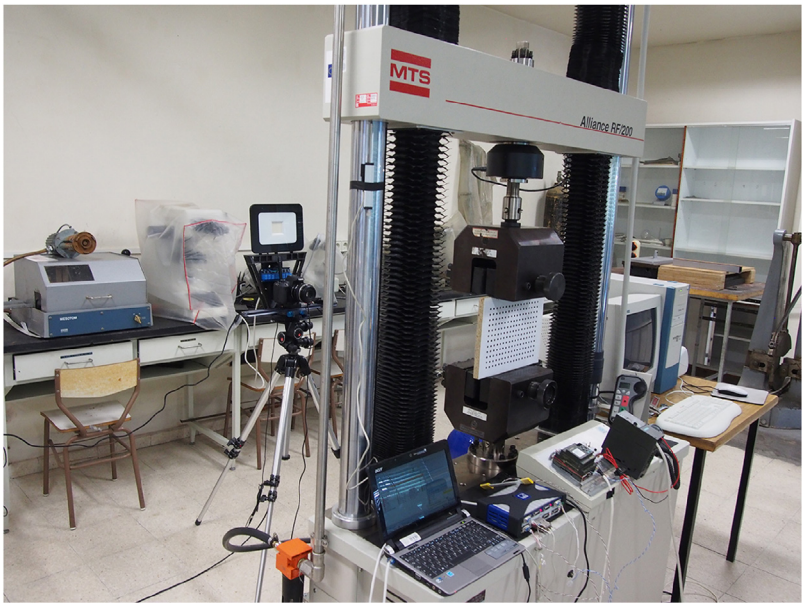

Fig. 5 – Disposition of the data acquisition system with respect to the traction testing machine.

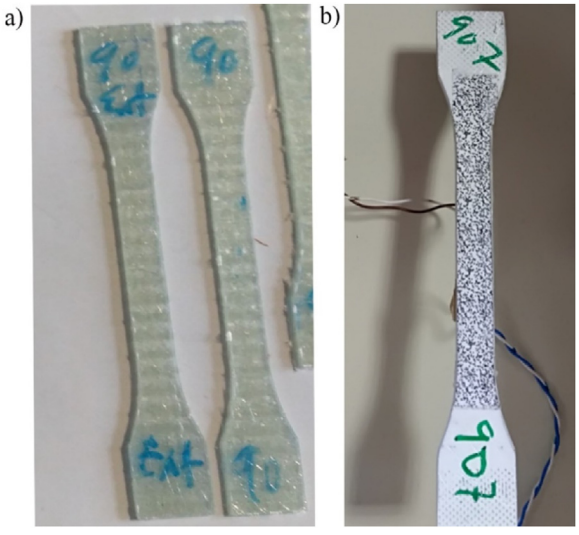

Fig. 6 – Composite specimens used during the experimental campaign: (a) natural texture of the tests specimens and (b) results after the application of the speckle pattern over the elastic white primer.

formed with standard technology which usually present a MIG of 40 [32].

$$MIG = \sum_{i=1}^{W}\sum_{j=1}^{H} \frac{|\nabla f(x_{ij})|}{W * H} \tag{3}$$

where $|\nabla f(x_{ij})|$ is the local intensity gradient vector of a gray-scale image, W is the width of the ROI and H is the height of the ROI.

For the camera calibration, a flat panel composed of 10×7 ring patterns (70 control points) with a grid distance of 25.4 mm was used (Fig. 7a). During this stage, a total of 18 images of the flat panel in different positions were acquired (Fig. 7b). Finally, the calibration approach shown in Section 2.2.2 was applied, allowing the estimation of the intrinsic camera parameters. These parameters were used to undistort the images acquired during the tensile tests.

3.2. *Full field displacements and strains*

Taking into consideration the step-up previously shown, a total of five tensile tests were carried out following the BS EN ISO 527-5:2009 guidelines [23]. On each test, the stretching speed of the traction testing machine was fixed at 2 mm/min, acquiring a total of 20 images (one image each 200 N of traction force increment). It is worth mentioning that the first camera

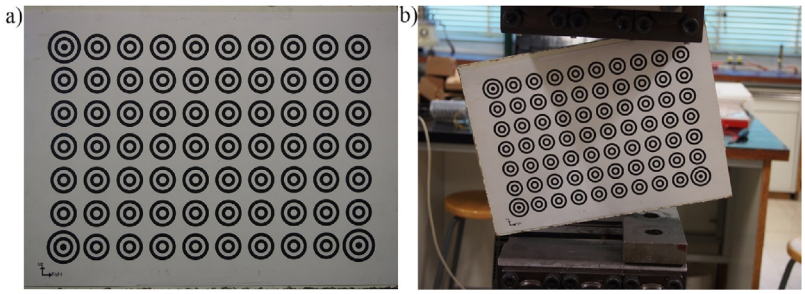

Fig. 7 – Geometrical calibration of the camera: (a) general view of the flat panel used for the calibration; (b) example of the positions used for the flat panel during the calibration.

shot was performed without load with the purpose of obtaining the reference image for the subsequent correlation process with the 2D-DIC method.

Then, each set of images were processed by means of the DIC approach defined in Section 2, using the open-source software Ncorr [33]. During this stage, a subset size of 50 × 50 pixels (approximately a square of 4 mm) with a step of 3 pixels was considered. This subset size ensures an adequate number of distinctive features for computing the ZNCC in each search window as well as a proper definition of the displacement field by means of linear shape functions (Fig. 2). As a result, it was possible to determine, on each test specimen, a full field of displacements (Fig. 8a) and strains (Fig. 8b and c).

Taking into consideration the type of test carried out, the state of stresses along the central area of the specimen can be considered constant and made up by an unique normal stress on the longitudinal direction. Therefore, if the material evaluated was homogeneous, the expected maximum principal strains will be constant. However, the results of the DIC analysis shown different maximum principal strains along the test specimen, highlighting the heterogeneous nature of the composite solution evaluated and thus the presence of different Young Modulus (Fig. 8b). Additional to this, it was possible to observe a variability in the minimum principal strain field suggesting the presence of a heterogeneous Poisson ratio (Fig. 8c). Both heterogeneities can be attributed

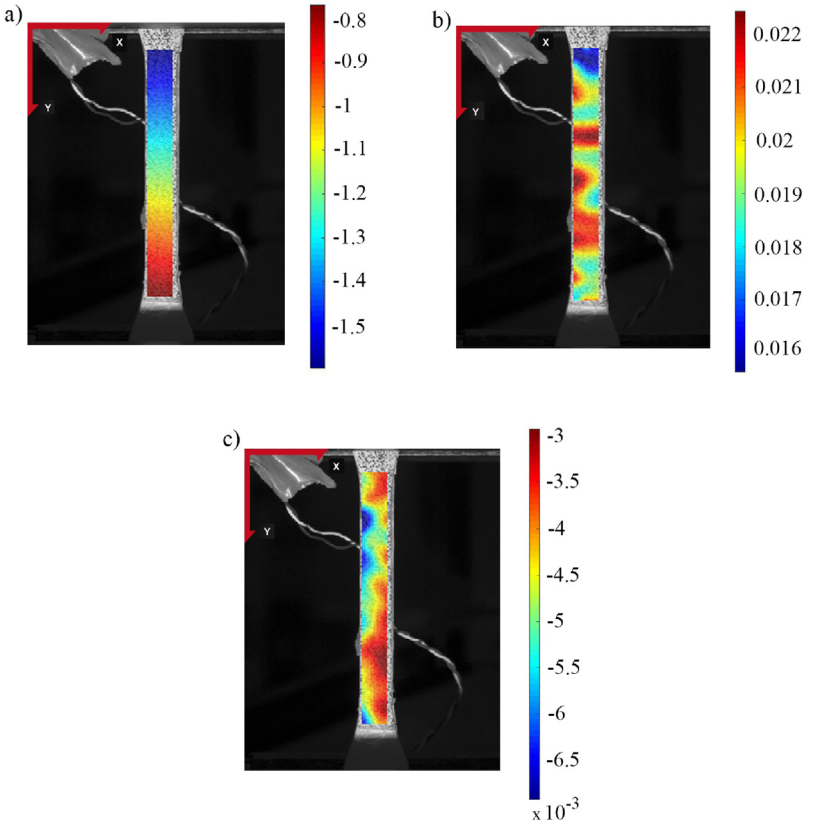

Fig. 8 – Detail of the displacements and strains obtained by the 2D-DIC method on the test specimens: (a) maximum displacements in mm in the *y*-axis direction; (b) maximum strains in the *y*-axis direction in mm/mm and (c) maximum strains in the *x*-axis direction in mm/mm.

to local variations during the production of the solution (small variations of the resin percentage in comparison with the fibre or small variations in the disposition of the fibres among other casuistics).

3.3. *Accuracy assessment*

With the aim of evaluating the accuracy provided by the 2D-DIC approach, in terms of displacements and strains, a LVDT (HBM TR50®) and a strain gauge (HBM-120 Ohm) were placed in one of the tests specimens used during the experimental method. Both sensors were connected with the data acquisition platform by means of the PLC system (Raspberry Pi-3® and Monarco HAT®). On the one hand, the data provided by the LVDT was contrasted with the displacements detected by the DIC approach between two fixed points (virtual extensometer) (Fig. 9a). It is worth mentioning that the application points of the virtual extensometer were the same than the measurement points of the LVDT in order to make the comparison reliable. On the other hand, the data provided by the strain gauge was compared with the strain obtained in the subset placed in the same area (Fig. 9a). During this comparison one image was captured each 100 N of Force (instead of the 200 N applied for the rest of the processes) with the aim of obtaining an enough number of points to compare both strains before the failure of the strain gauge. In order to compare both strains the data provided by the strain gauge (engineering strains) was transformed to the Green–Lagragian strain tensor in order to be compared with the strain data provided by the 2D-DIC.

The data recorded from the extensometer and the strain gauges revealed an average discrepancy of 0.02 mm (0.32 pixels) for the displacements and 0.0002 mm/mm for the strains in the longitudinal direction regarding the displacements and the strains obtained by the 2D-DIC approach (Fig. 9b and c). These values correspond with a root-mean-square error (RMSE) of 2.97% for the displacements and a RMSE of 0.04% for the strains. Therefore, these lower discrepancies demonstrate the feasibility and accuracy of the 2D-DIC method as well as the data acquisition of the prototype.

3.4. *Mechanical properties of the composite solution evaluated*

The mechanical characterization of the composite solution can be carried out confronting the data provided by the virtual extensometers placed on the test specimen and the stresses captured by the DIC prototype (the strain–stress curve) (Figs. 9 and 10a). These stresses were the result of the force applied by

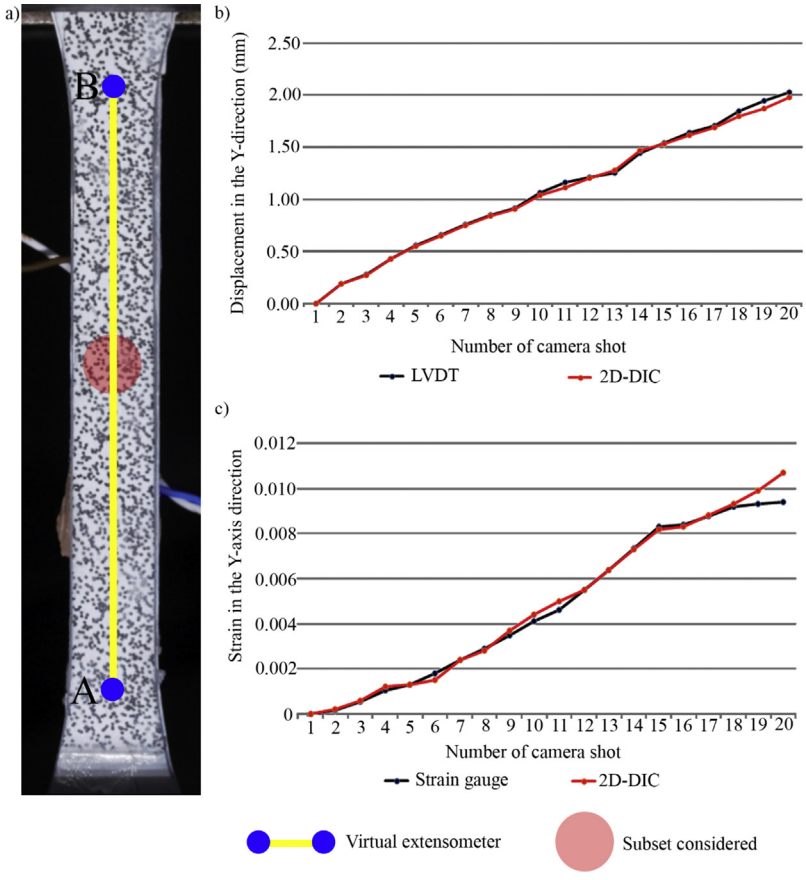

Fig. 9 – Results of the tensile test used to check the accuracy of the method: (a) location of the virtual extensometer and subset considered; (b) graphical comparison between the extensometer and the displacements obtained by the virtual extensometer through the 2D-DIC method and (c) graphical comparison between the strain gauge and the displacements obtained by the virtual extensometer through the 2D-DIC method.

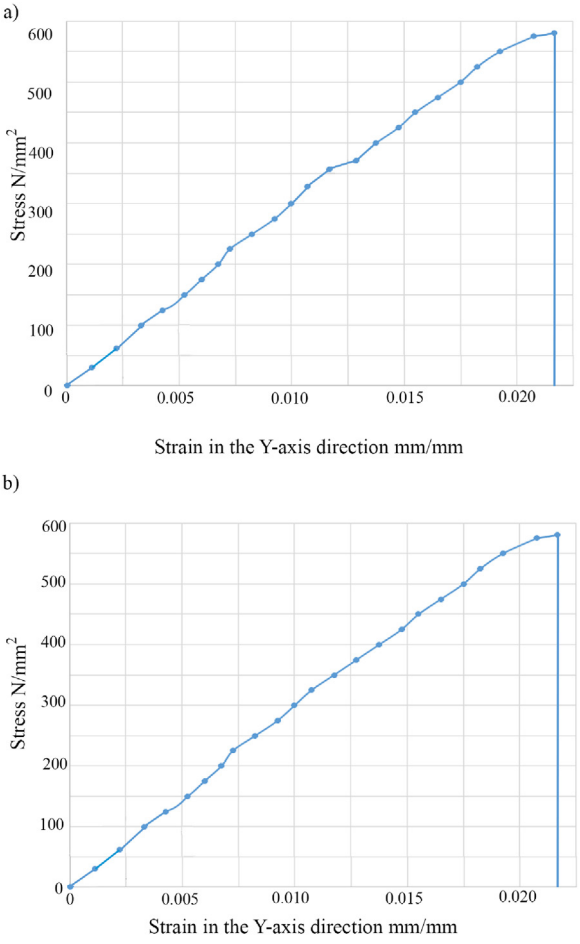

Fig. 10 – Example of a strain–stress curve obtained during the tensile tests: (a) strain–stress from the testing machine and; (b) strain–stress curve obtained from the virtual extensometers.

the press and the area of the test specimen (10 mm × 2 mm). The strain–stress curves obtained by the press and the DIC approach shown a composite solution with a marked brittle behaviour (absence of plasticity) and a linear elastic behaviour (Fig. 10).

It is worth mentioning that the characterization of the material's mechanical properties by means of virtual extensometers allowed the proper definition of the composite solution from a deterministic point of view (considering the composite material as homogeneous). However, the results obtained by the DIC approach highlight the presence of a heterogeneous solution (Fig. 8).

Taking into account that one of the main advantages offered by the DIC approach is the full field strain characterization, it was possible to extract the probabilistic density distributions of each mechanical property that define the composite solution and thus capturing the heterogeneity shown by the material. To this end, the full-field strains obtained by the DIC approach were transformed into Young's Modulus and Poisson's ratios by means of a convolution process as follows (Fig. 11): (i) definition of the kernel matrix; (ii) convolution along the entire ROI defined by m steps along the horizontal direction and n steps along the vertical direction; (iii) obtention of the Young's Modulus of each area evaluated confronting the maximum strain values obtained in each cycle by the convolution and the stress registered by the DIC prototype; (iv) evaluation of the Poisson's ratio by means of the relation between the maximum and minimum strain obtained by the convolution process. For the present study case, it was considered as kernel size similar to the size of the finite element used for the numerical simulations (50 × 50 pixels) and a step between kernels of 50 pixels in order to avoid overlaps.

Apart from the elastic properties of the composite solution, Young's Modulus and Poisson ratio, the maximum principal strain (yield strain) was calculated with the aim of defining properly the constitutive material model by means of the Tsai–Wu criterion [34]. To this end, a new ROI was defined on the observed failure area of each test specimen (Fig. 11). Then, it was applied the same procedure than those proposed for the extraction of the Elastic Modulus and Poisson ratio.

The parameters extracted by the convolution process previously defined allowed the creation of a population for each variable (Table 6). These parameters correspond to the material 0° mechanical properties. Because the number of layers and the direction of the reinforcement on each layer, they coincide with the mechanical properties of the material at 90° (Table 4).

With the aim of obtaining the probabilistic distribution function (PDF) of each variable a normality tests, by means of the Shapiro–Wilk approach, was carried out [35]. This test allowed us to characterize the populations into normal and non-normal distributions (Table 7). Finally, a curve fit method was performed with the aim of obtaining the PDFs. The candidate PDFs considered were Normal, Log-Normal, Weibull, Exponential and Uniform, obtaining normal distribution for the Young's Modulus and Poisson ratio and a Weibull distribution for the maximum principal strain (Table 5 and Fig. 12). These curves are consistent with the PDFs obtained in other experimental campaigns methodologies [13].

4. Numerical simulation combining DIC and stochastic approaches

4.1. *Definition of the numerical model*

In order to integrate the data provided by the DIC method with advance numerical simulations of composite pressure vessels, a prototype was created with the commercial finite element software ABAQUS®. This receptacle was designed with a semi-spherical shape in the upper and lower part and a cylindrical shape for the body of the container (Fig. 13). All these parts were designed with an internal radius of 16.5 mm and a constant thickness of 2 mm. For the body of the vessel, a height of 307 mm was considered.

Taking into consideration the geometrical model defined previously, two numerical meshes, composed of 10,368 first order quadrilateral shell elements (10,464 nodes and 62,784 degrees of freedom), were generated, namely (Fig. 14): (i) deterministic mesh and (ii) probabilistic mesh. While, the deterministic mesh considers the mechanical properties of the

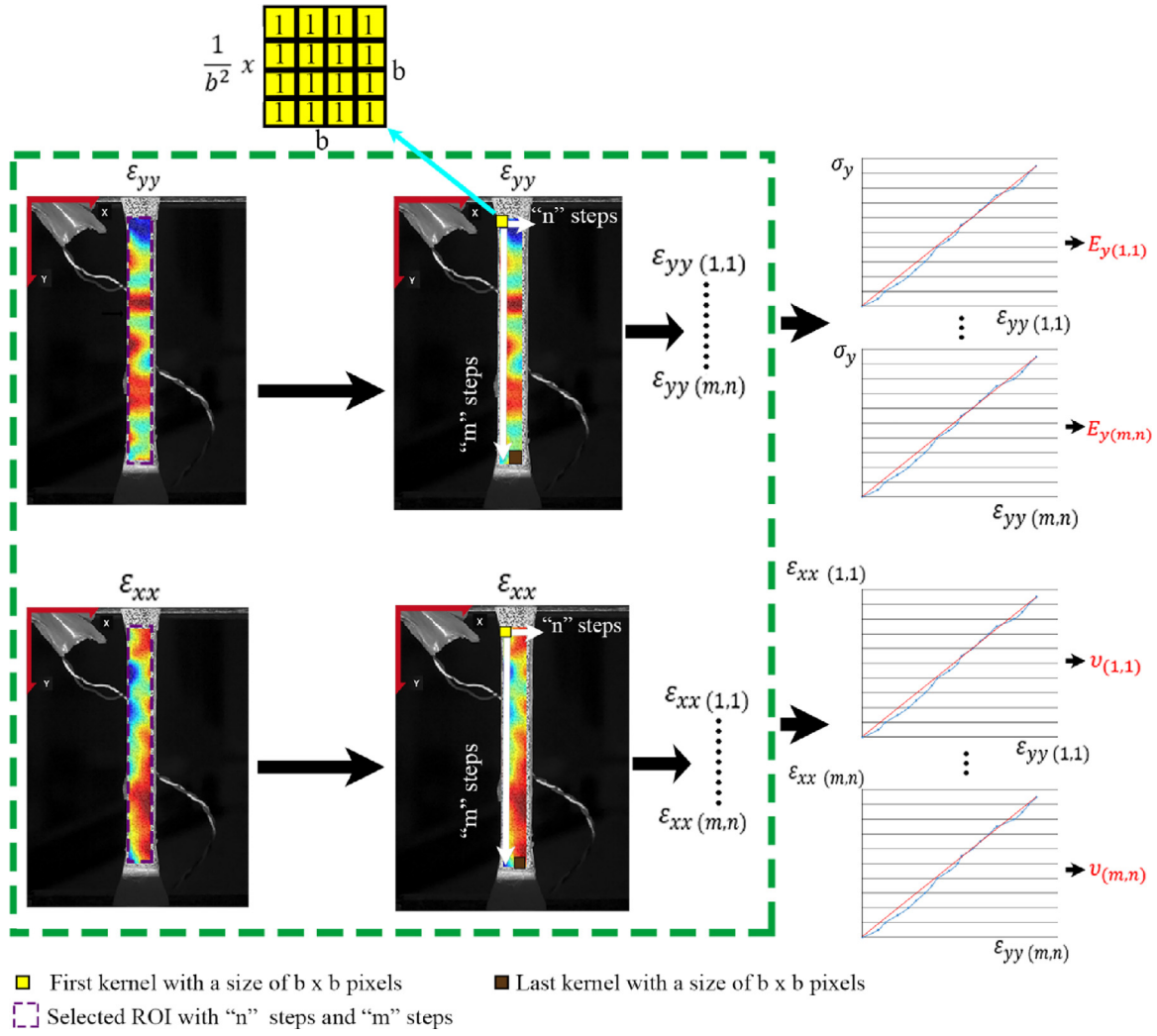

Fig. 11 – Proposed workflow to obtain the Young Modulus (E_y) and the Poisson ratios (υ) of the specimens. The green line indicates one cycle on each deformed image.

composite material as unique and homogeneous, the probabilistic mesh represents the composite material as an heterogeneous material whose mechanical properties are extracted from the PDF obtained from the DIC approach (Fig. 12).

For all the numerical simulations, the following considerations were taken into account: (i) a uniform service pressure of 3 MPa according to guidelines [36]; (ii) a planar state of stresses without shear components (thin shell theory); (iii) a symmetrical Young's Modulus due to the symmetrical disposition of the fibres (Fig. 1) and; (iv) a failure criterion based on the Tsai–Wu theory [34].

4.2. *Global sensitivity analysis*

4.2.1. *Polynomial chaos expansion and the Sobol' method*

Prior to the numerical evaluation, a sensitivity analysis was carried out with the aim of evaluating the influence of the input parameters in the model response (Tsai–Wu failure criterion). Among the variety of methods used in sensitivity analysis, one of the most common and robust is the Sobol' method [37,38]. This method is based on the decomposition of the response variance as a sum of contributions related to each input parameter through the Sobol's indices, which are usually assessed through the use of Monte Carlo (MC) simulations.

Table 5 – Probabilistic distribution functions of the elastic modulus, Poisson's ratio and strain in the y-axis direction of the specimens.

Parameter	Distribution	*p*-Value	Mean (Normal)/A (Weibull)	Deviation (Normal)/B (Weibull)
Young's Modulus (GPa)	Normal	0.99	27.11	1.24
Poisson's ratio (–)	Normal	0.97	0.21	0.03
y-Axis strain (mm/mm)	Weibull	0.21	0.02	14.74

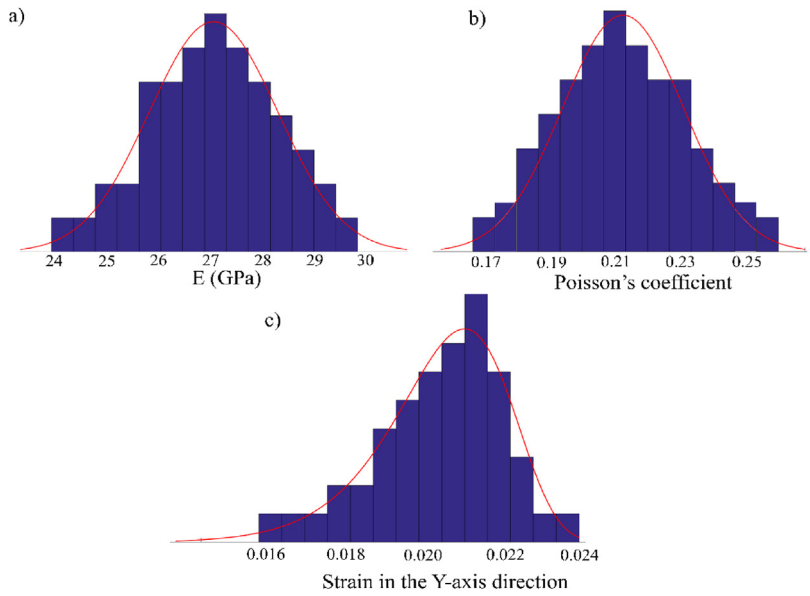

Fig. 12 – Graphical representation of the probabilistic distribution functions of each parameter: (a) normal distribution of the elastic modulus; (b) normal distribution of the Poisson's coefficient and (c) Weibull distribution of the maximum principal strain.

However, the MC simulations require thousand of simulations to achieve reliable results [39]. Considering this topic, there is an alternative that offers reliable results with lower computational cost: the so-called subrrogate models. The main advantages of these models are their compactness and their analytical scalability, allowing to approximate the input–output response of a complex system with a low number of inputs.

From the present study case, the polynomial chaos expansion (PCE) metamodel was used. This strategy approximates the computational model through a set of orthonormal polynomials of the input parameters (Eq. (4)) [40]. Complementary to this, a least-angle regression and a least-square minimization were used with the aim of determining the coefficients of the polynomials (Eq. (4)) [41].

$$\tilde{f} = \sum_{\alpha \in A} y_\alpha \psi_\alpha(X) \tag{4}$$

where $\tilde{f}$ is the subrrogate model, $\alpha = \{\alpha_1 \cdots \alpha_d\}$ are the indexes of the PCE, A is the set of indexes α which correspond to the truncation scheme, $X = (X_1, X_2, \ldots, X_d)$ is the multivariate vector of the input parameters considered and finally, ψ_α is the multivariate polynomial.

In order to validate the accuracy of the metamodel, the leave-one-out error (LOO) was used [42,43]. Once the metamodel was built and validated, the first and total Sobol's indices were calculated through Eqs. (5) and (6), respectively.

$$\hat{S}_i = \frac{\sum_{\alpha \in A} \hat{y}_\alpha^2}{\sum_{\alpha \in A, \alpha \neq 0} \hat{y}_\alpha^2} \quad \text{where } A_i = \{\alpha \in A : \alpha_i > 0,\ \alpha_{j \neq i} = 0\} \tag{5}$$

$$\hat{S}_i^t = \frac{\sum_{\alpha \in At} \hat{y}_\alpha^2}{\sum_{\alpha \in A, \alpha \neq 0} \hat{y}_\alpha^2} \mathbf{af}; \quad \text{where } A_i^T = \{\alpha \in A : \alpha_i > 0\} \tag{6}$$

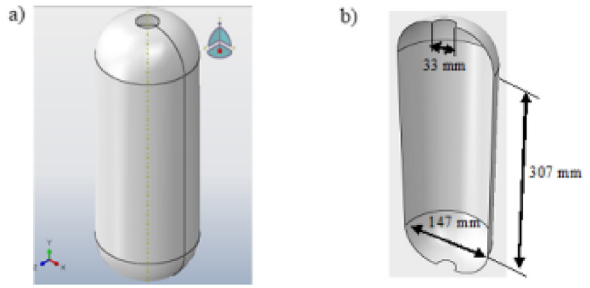

Fig. 13 – Pressure vessel evaluated: (a) general view and (b) cross section.

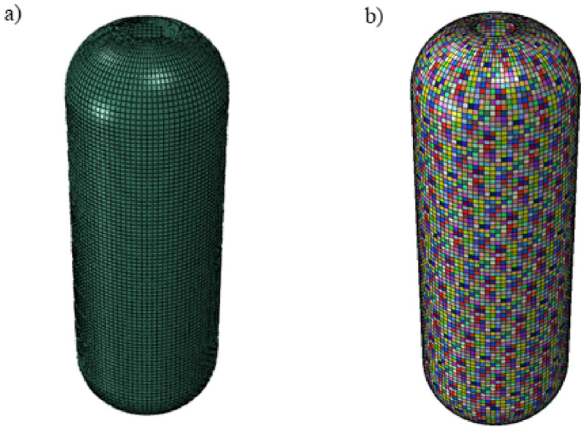

Fig. 14 – Numerical meshes considered: (a) deterministic mesh and (b) probabilistic mesh. The size of the elements was 4 mm, corresponding with the subset size used during the DIC tests. In different colours the materials considered for each numerical simulation.

where $\hat{S}_i$ and $\hat{S}_i^t$ are the first-order and total Sobol's indices of the output variable i, $\hat{y}$ and α are the coefficients and indices of the PCE respectively and A is the subset of the input variables.

4.2.2. *Results obtained from the global sensitivity analysis*

Taking into account the methodology described in the previous section, a global sensitivity analysis was performed over the deterministic mesh, considering as input variables those obtained by the DIC approach, namely: (i) Young Modulus; (ii) Poisson's coefficient and (iii) maximum principal strain.

Once these set of variables were, different PCE-metamodels were built in order to assess the Sobol's indices of the output: the Tsai–Wu factor. During these assessments different sample sizes were considered with the purpose of obtaining the best ratio between the number of samples and the consistency of the metamodel. These samples were obtained through the use of the latin hypercube sampling (LHS) method [44] taking into account the PDF of each variable (Table 5 and Fig. 12).

The results revealed that the optimum design of experiment (DoE) of the metamodel was 200, showing a LOO error of 1.44×10^{-4} (Table 6) and a constant value in the different Sobol's indexes (Table 7).

From the Sobol's analysis it is possible to conclude that the uncertainties associated with the Tsai–Wu factor are mainly due to the maximum principal strain (e_{11}) (Fig. 15). This variable influences approximately 76% of the total variation of this factor, being consistent with the formulation of the Tsai–Wu criterion [34]. Also, it is possible to observe a high sensitivity of the Young's Modulus (E) in the final results, which influences 16% of the uncertainty of the Tsai–Wu factor. The Poisson ratio is the less sensitive variable (Fig. 15). It is worth mentioning that the First Order Sobol indexes were similar to the total Sobol indexes, suggesting that there is no interaction between variables (Fig. 15).

4.3. *Stochastic analysis*

Taking into consideration that the safety of a composite pressure vessel is guaranteed when the Tsai–Wu factor is lower than 1, a robust numerical analysis passes through the use of a stochastic approach able to integrate the uncertainty of the inputs, obtained by means of the DIC approach, in order to determine the probability of having a specific range of Tsai–Wu factors. On this basis, the Semi Random Field method (random variable approach) proposed by [45] was adopted (Fig. 16). In this approach, each element of the numerical model adopts random values of the variables (Young's Modulus, Poisson's coefficient and maximum principal strain) according to the probability density functions obtained by means of the DIC approach (Fig. 12 and Table 5).

Table 6 – LOO error in the output variable (Tsai–Wu failure criterion) for different sizes of the DoE.

Number of samples obtained with the LHS	LOO error
25	11.1
50	0.98
100	1.22×10^{-3}
200	1.44×10^{-4}
300	1.58×10^{-5}
400	4.10×10^{-6}

Table 7 – Total Sobol's indices obtained of the output variable (Tsai–Wu failure criterion) of the pressure vessel during the global sensitivity analysis.

	Total Sobol's indices		
Number of samples obtained with the LHS	Elastic modulus	Poisson's coefficient	Maximum principal strain
25	0.17	0.06	0.77
50	0.21	0.05	0.74
100	0.17	0.08	0.75
200	0.16	0.08	0.76
300	0.16	0.08	0.76
400	0.16	0.08	0.76

Considering that the input uncertainties in the output values in complex system can be written as exposed bellow (Eq. (7)), the probability of having a value lower than a pre-establish threshold can be defined by means of the complementary cumulative distribution function (CCDF) (Eqs. (7) and (8)).

$$Y_i = f(D_i * X_i) \tag{7}$$

$$prob(y > Y) = \int_{S_{SU}} \delta Y[f(x)] pdf_u(X) dV_{SU} \tag{8}$$

where f represents the numerical model, X_i the input vector; D_i the distribution associated with each element of the numerical model and Y_i the model's predictions.

It is worth mentioning that the value of this integral is not trivial, requiring the use of approximation methods such as the Fourier amplitude sensitivity test (FAST) or the Monte Carlo simulation. For the present study case, the LHS method was used to estimate the propagation and analysis of the uncertainty of the output values [46]. Specifically, a total of 500 samples were used to create the PDF and the CCDF of the Tasi–Wu values (Fig. 17).

Considering a value of 0.95 as an acceptable probability level, the most unfavourable case during the design of this pressure vessel will be 0.54 (maximum admissible pressure of 5.56 MPa), meanwhile in the most favourable case, the pressure vessel will have a value of 0.39 (maximum admissible pressure of 7.69 MPa), with 0.46 and 6.52 MPa being the most probable value for the Tsai–Wu and the maximum pressure respectively (Fig. 17a). These results contrast with those obtained by means of a deterministic model (numerical model generated with the average values of each variable), for which a Tsai–Wu factor of 0.37 was obtained (Fig. 17b). These values threw a maximum admissible pressure of 8.10 MPa. In this case, the maximum pressure is achieved at the same time in all those elements placed close to the nozzle's hole in the

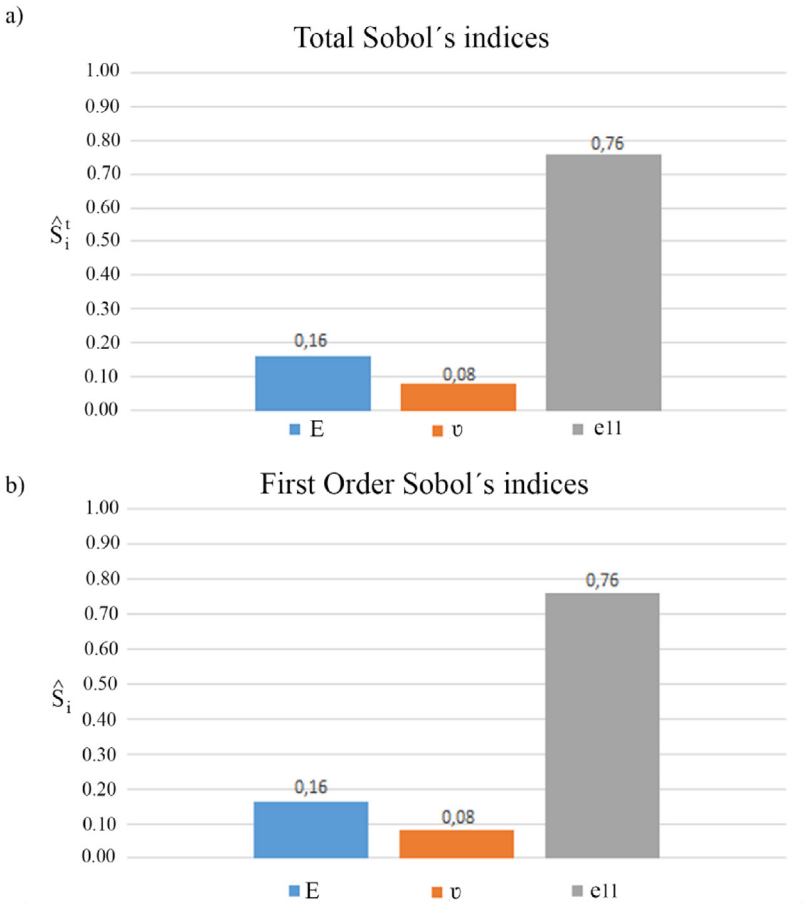

Fig. 15 – Results obtained from the PCE metamodel: (a) total Sobol indices ($\hat{S}_i^t$) and (b) first Order Sobol indices ($\hat{S}_i$).

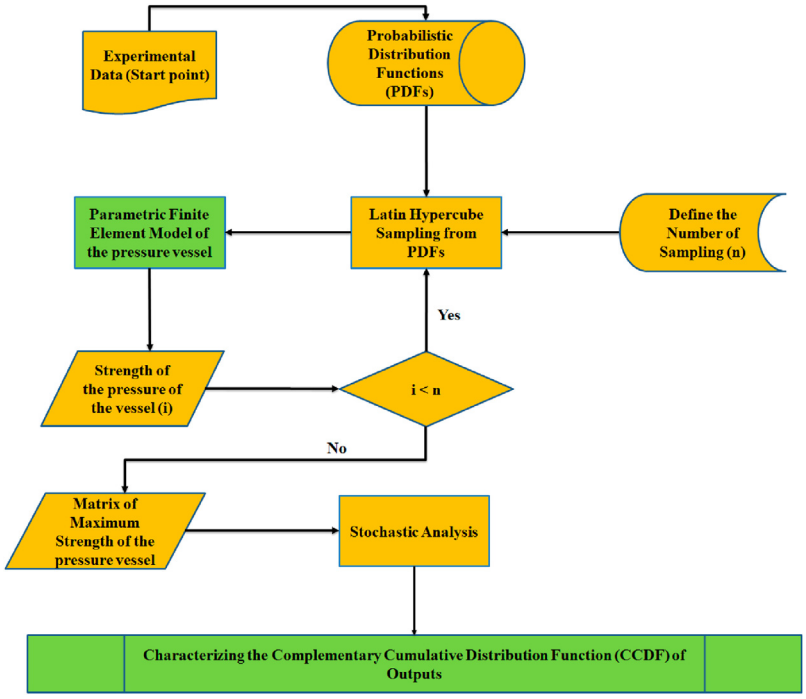

Fig. 16 – Workflow adopted for the stochastic evaluation of the composite pressure vessel.

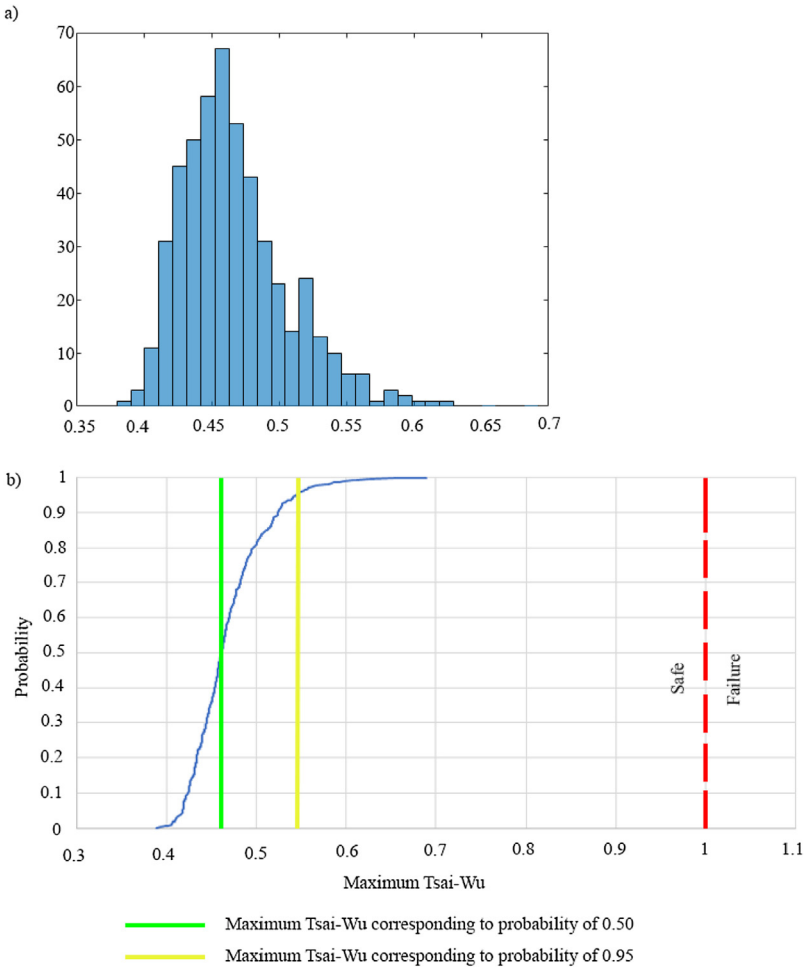

Fig. 17 – Results of the semi-random field simulation: (a) complementary cumulative density function and (b) probabilistic density function.

spherical part of the vessel (Fig. 18a). In contrast with this, the probabilistic model obtained a random distribution of the

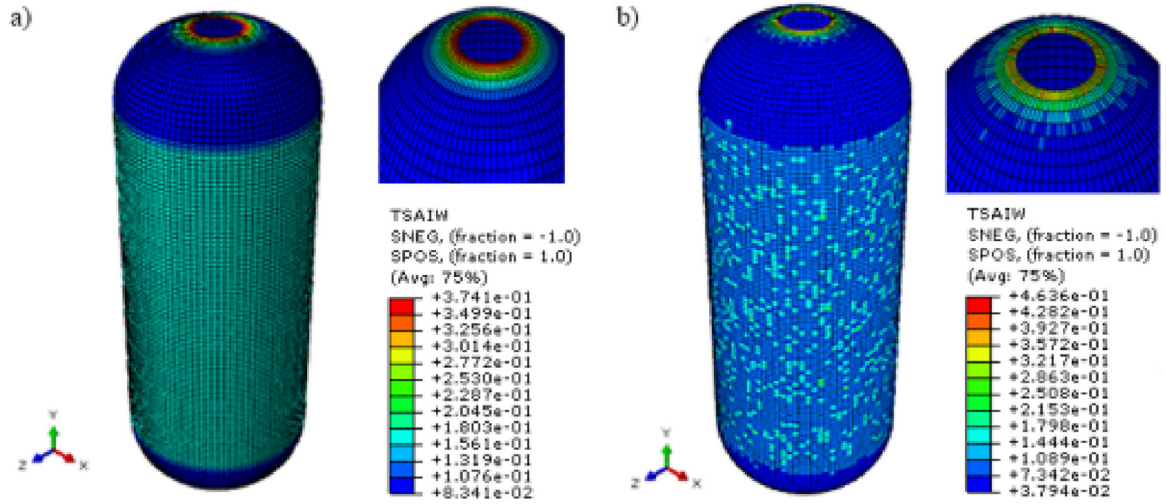

Fig. 18 – Numerical results: (a) deterministic model built with the average values and (b) example of a sample used during the probabilistic analysis.

Tsai–Wu factor, highlighting the probability of a random fracture which depends of the local mechanical properties of the composite material (Fig. 18b).

5. Conclusions

This paper proposes a methodology based on the combination of the 2D digital image correlation method with probabilistic approaches, based on random variable strategy, with the purpose of obtaining a reliability analysis of composite pressure vessels. To this end, it is proposed a methodology able to exploit the full field data provided by the 2D digital image correlation method with the aim of obtaining the probabilistic density function of each material property, namely: (i) Young's Modulus; (ii) Poisson's ratio and; (iii) Yield Strain. Then, and with the aim of integrating this data into an advanced numerical framework, two finite element models of a pressure vessel prototype were built: (i) a deterministic model and; (ii) a probabilistic model. On the one hand, the deterministic model was used to study the influence of the input uncertainties in the output values (Tsai–Wu safety factor), suggesting that the Tsai–Wu factor is mainly influenced by the maximum strain and the Young Modulus. On the other hand, the probabilisitic model was used to study, from a stochastic point of view, the safety factor of the pressure vessel prototype, adopting to this end a Monte Carlo strategy based on the Latin Hypercube Sampling method. This approach, fed by the probabilistic functions, threw more conservative values than for the deterministic one. These differences can be attributed, mainly, to the uncertainties in the maximum principal strain with an average value of 0.021 mm/mm and a covariance value of 15.69%, specially in the union between the vessel's body and the vessel's nozzle. In this area, the fracture in the deterministic model is obtained at the same time on all points, meanwhile in the probabilistic model is obtained in one point (area with the worst mechanical properties). Taking into consideration the results obtained during the experimental campaign, future works will be focused on the following fields: (i) on the use of the full field data provided by DIC for the estimation of the correlation functions needed for the creation of random fields models in composite materials; (ii) on the improvement of the methodology used to design the speckle pattern including additional restriction that improve the heterogeneity of the gray level values and thus increase the MIG value of the ROI; (iii) the integration of the 3D DIC approach for the validation of the solution developed by the stochastic strategy shown in this paper.

Conflict of interest

None declared.

Ethical statement

This material has not been published in whole or part elsewhere.

The manuscript is not currently being considered for publication in another journal.

All authors have been personally and actively involved in substantive work leading to the manuscript.

Funding body

This work was financed by ERDF funds through the V Sudoe Interreg program within the framework of the COMPRESSer project, Ref. SOE2/P1/E0643 and the TCUE action SICMES supported by the Foundation University of Salamanca.

Acknowledgments

The authors would like to thank the V Sudoe Interreg program and the TCUE action SICMES.

REFERENCES

[1] M. Delogu, L. Zanchi, C. Dattilo, M. Pierini, Innovative composites and hybrid materials for electric vehicles lightweight design in a sustainability perspective, Mater. Today Commun. 13 (2017) 192–209, https://doi.org/10.1016/j.mtcomm.2017.09.012.

[2] A. Vicario, S.S. Ramanan, S. Arun, 3.4 Composites in Missiles and Launch Vehicles, 2018.

[3] L. Sutherland, A review of impact testing on marine composite materials: Part I – marine impacts on marine composites, Compos. Struct. (2017), https://doi.org/10.1016/j.compstruct.12.073.

[4] R.F. Gibson, A review of recent research on mechanics of multifunctional composite materials and structures, Compos. Struct. 92 (2010) 2793–2810, https://doi.org/10.1016/j.compstruct.2010.05.003.

[5] R. Rafiee, M.A. Torabi, Stochastic prediction of burst pressure in composite pressure vessels, Compos. Struct. 185 (2018) 573–583, https://doi.org/10.1016/j.compstruct.2017.11.068.

[6] L.J. Sánchez-Aparicio, L.F. Ramos, J. Sena-Cruz, J.O. Barros, B. Riveiro, Experimental and numerical approaches for structural assessment in new footbridge designs (SFRSCC–GFPR hybrid structure), Compos. Struct. 134 (2015) 95–105, https://doi.org/10.1016/j.compstruct.2015.07.041.

[7] N. Movahedi, E. Linul, Mechanical properties of light expanded clay aggregated (LECA) filled tubes, Mater. Lett. 217 (2018) 194–197, https://doi.org/10.1016/j.matlet.2018.01.078.

[8] E. Linul, L. Marsavina, J. Kováčik, Collapse mechanisms of metal foam matrix composites under static and dynamic loading conditions, Mater. Sci. Eng.: A 690 (2017) 214–224, https://doi.org/10.1016/j.msea.2017.03.009.

[9] T. Fiedler, M. Taherishargh, L. Krstulović-Opara, M. Vesenjak, Dynamic compressive loading of expanded perlite/aluminum syntactic foam, Mater. Sci. Eng.: A 626 (2015) 296–304, https://doi.org/10.1016/j.msea.2014.12.032.

[10] R. Rafiee, On the mechanical performance of glass-fibre-reinforced thermosetting-resin pipes: a review, Compos. Struct. 143 (2016) 151–164, https://doi.org/10.1016/j.compstruct.2016.02.037.

[11] S. Sriramula, M.K. Chryssanthopoulos, Quantification of uncertainty modelling in stochastic analysis of FRP

composites, Compos. Part A: Appl. Sci. Manufact. 40 (2009) 1673–1684, https://doi.org/10.1016/j.compositesa.2009.08.020.
[12] J.N. Reddy, Mechanics of Laminated Composite Plates and Shells: Theory and Analysis, CRC Press, 2004.
[13] P. Sasikumar, R. Suresh, P. Vijayaghosh, S. Gupta, Experimental characterisation of random field models for CFRP composite panels, Compos. Struct. 120 (2015) 451–471, https://doi.org/10.1016/j.compstruct.2014.10.023.
[14] O. Orell, J. Vuorinen, J. Jokinen, H. Kettunen, P. Hytönen, J. Turunen, et al., Characterization of elastic constants of anisotropic composites in compression using digital image correlation, Compos. Struct. 185 (2018) 176–185, https://doi.org/10.1016/j.compstruct.2017.11.008.
[15] M. Tekieli, S. De Santis, G. de Felice, A. Kwiecień, F. Roscini, Application of digital image correlation to composite reinforcements testing, Compos. Struct. 160 (2017) 670–688, https://doi.org/10.1016/j.compstruct.2016.10.096.
[16] S. Sharifi, S. Gohari, M. Sharifiteshnizi, R. Alebrahim, C. Burvill, Y. Yahya, et al., Fracture of laminated woven GFRP composite pressure vessels under combined low-velocity impact and internal pressure, Arch. Civil Mech. Eng. 18 (2018) 1715–1728, https://doi.org/10.1016/j.acme.2018.07.006.
[17] M.A. Seif, U.A. Khashaba, R. Rojas-Oviedo, Measuring delamination in carbon/epoxy composites using a shadow moiré laser based imaging technique, Compos. Struct. 79 (2007) 113–118, https://doi.org/10.1016/j.compstruct.2005.11.039.
[18] P. Callaway, M. Gilbert, C.C. Smith, Influence of backfill on the capacity of masonry arch bridges, in: Proceedings of the Institution of Civil Engineers: Bridge Engineering, ICE Publishing, 2012 147–157, https://doi.org/10.1680/bren.11.00038.
[19] F. Hild, S. Roux, Digital image correlation: from displacement measurement to identification of elastic properties – a review, Strain 42 (2006) 69–80, https://doi.org/10.1111/j.1475-1305.2006.00258.x.
[20] H.C. Biscaia, N. Franco, C. Chastre, Development of a simple bond-slip model for joints monitored with the DIC technique, Arch. Civil Mech. Eng. 18 (2018) 1535–1546, https://doi.org/10.1016/j.acme.2018.06.009.
[21] L.J. Sánchez-Aparicio, A. Villarino, J. García-Gago, D. González-Aguilera, Photogrammetric, geometrical, and numerical strategies to evaluate initial and current conditions in historical constructions: a test case in the church of San Lorenzo (Zamora, Spain), Remote Sensing 8 (2016), http://dx.doi.org/10.3390/rs8010060.60.
[22] T. Gajewski, T. Garbowski, Calibration of concrete parameters based on digital image correlation and inverse analysis, Arch. Civil Mech. Eng. 14 (2014) 170–180, https://doi.org/10.1016/j.acme.2013.05.012.
[23] ISOB, Plastics – Determination of Tensile Properties, 1997.
[24] B. Pan, K. Qian, H. Xie, A. Asundi, Two-dimensional digital image correlation for in-plane displacement and strain measurement: a review, Meas. Sci. Technol. 20 (2009) 062001, http://dx.doi.org/10.1088/0957-0233/20/6/062001.
[25] L. Luu, Z. Wang, M. Vo, T. Hoang, J. Ma, Accuracy enhancement of digital image correlation with B-spline interpolation, Opt. Lett. 36 (2011) 3070–3072, https://doi.org/10.1364/OL.36.003070.
[26] J. Blaber, B. Adair, A. Antoniou, Ncorr: open-source 2D digital image correlation matlab software, Exp. Mech. 55 (2015) 1105–1122. , http://dx.doi.org/10.1007/s11340-015-0009-1.
[27] B. Pan, Reliability-guided digital image correlation for image deformation measurement, Appl. Opt. 48 (2009) 1535–1542, https://doi.org/10.1364/AO.48.001535.
[28] Y. Dong, B. Pan, A review of speckle pattern fabrication and assessment for digital image correlation, Exp. Mech. 57 (2017) 1161–1181. , http://dx.doi.org/10.1007/s11340-017-0283-1.
[29] Z. Chen, C. Quan, F. Zhu, X. He, A method to transfer speckle patterns for digital image correlation, Meas. Sci. Technol. 26 (2015) 095201, http://dx.doi.org/10.1088/0957-0233/26/9/095201.
[30] M.N. Vo, Z. Wang, L. Luu, J. Ma, Advanced geometric camera calibration for machine vision, Opt. Eng. 50 (2011) 110503, https://doi.org/10.1117/1.3647521.
[31] D. Lecompte, H. Sol, J. Vantomme, A. Habraken, Analysis of speckle patterns for deformation measurements by digital image correlation, in: SPECKLE06: Speckles, From Grains to Flowers: International Society for Optics and Photonics, 2006, 63410E, https://doi.org/10.1117/12.695276.
[32] B. Pan, Z. Lu, H. Xie, Mean intensity gradient: an effective global parameter for quality assessment of the speckle patterns used in digital image correlation, Opt. Lasers Eng. 48 (2010) 469–477, https://doi.org/10.1016/j.optlaseng.2009.08.010.
[33] A. Ab Ghani, M. Ali, S. Dharmalingam, J. Mahmud, Digital Image Correlation (DIC) Technique in Measuring Strain Using Opensource Platform Ncorr, 2016.
[34] S.W. Tsai, E.M. Wu, A general theory of strength for anisotropic materials, J. Compos. Mater. 5 (1971) 58–80, https://doi.org/10.1177/002199837100500106.
[35] S.S. Shapiro, M.B. Wilk, An analysis of variance test for normality (complete samples), Biometrika 52 (1965) 591–611. , http://dx.doi.org/10.2307/2333709.
[36] Certificación AEdNy, UNE-EN 3-8: extintores portátiles de incendios. Requisitos adicionales a la Norma Europea EN 3-7 para la construcción resistencia a la presión y los ensayos mecánicos para extintores con una presión máxima admisible igual o inferior a 30 bar, AENOR, 2007.
[37] IyM. Sobol', On sensitivity estimation for nonlinear mathematical models, Matematich. Model. 2 (1990) 112–118.
[38] F. Zhu, Q. Zhou, F. Wang, X. Yang, Spatial variability and sensitivity analysis on the compressive strength of hollow concrete block masonry wallettes, Construct. Build. Mater. 140 (2017) 129–138, https://doi.org/10.1016/j.conbuildmat.2017.02.099.
[39] B. Sudret, Global sensitivity analysis using polynomial chaos expansions, Reliab. Eng. Syst. Saf. 93 (2008) 964–979, https://doi.org/10.1016/j.ress.2007.04.002.
[40] R. Ghanem, P. Spanos, Stochastic Finite Elements: A Spectral Approach, revised edition, Dover Publications, New York, 2003.
[41] G. Blatman, B. Sudret, Adaptive sparse polynomial chaos expansion based on least angle regression, J. Comput. Phys. 230 (2011) 2345–2367, https://doi.org/10.1016/j.jcp.2010.12.021.
[42] M. Stone, Cross-validatory choice and assessment of statistical predictions, J. R. Stat. Soc. Ser. B (Methodol.) (1974) 111–147.
[43] S. Geisser, The predictive sample reuse method with applications, J. Am. Stat. Assoc. 70 (1975) 320–328.
[44] M.D. McKay, R.J. Beckman, W.J. Conover, Comparison of three methods for selecting values of input variables in the analysis of output from a computer code, Technometrics 21 (1979) 239–245, https://doi.org/10.1080/00401706.1979.10489755.
[45] E. Moradabadi, D.F. Laefer, J.A. Clarke, P.B. Lourenço, A semi-random field finite element method to predict the maximum eccentric compressive load for masonry prisms, Construct. Build. Mater. 77 (2015) 489–500, https://doi.org/10.1016/j.conbuildmat.2014.12.027.
[46] J.C. Helton, F.J. Davis, Latin hypercube sampling and the propagation of uncertainty in analyses of complex systems, Reliab. Eng. Syst. Saf. 81 (2003) 23–69, https://doi.org/10.1016/S0951-8320(03)00058-9.